A Model for Supersaturation and Aspect Ratio for Growth Dominated Crystallization from Solution

Lotfi Derdour
Particle Science, Devices and Engineering, GlaxoSmithKline, King of Prussia, PA 19406

Eric J. Chan
Drug Product Science and Technology, Bristol-Myers Squibb, Co., New Brunswick, NJ 08901

DOI 10.1002/aic.15007
Published online August 22, 2015 in Wiley Online Library (wileyonlinelibrary.com)

A model for predicting supersaturation, crystal growth rate, crystal size distribution, and aspect ratio is presented. The model applies to isothermal anti-solvent crystallization where crystal growth is the dominant phenomena and for systems where crystal habit can be characterized by two-dimensional variables. A parameter estimation algorithm was derived to extract solute integration coefficients in the two growth directions from experimental data about temporal evolution of concentration during crystallization, the final aspect ratio, and the aspect ratio at the end of the seed age period. Model's predictions for supersaturation and aspect ratio were in good agreement with experimental data obtained on an investigational drug that crystallizes in the parallelepipedic shape. Finally, model simulations predict that for a given initial seed size, the seed loading is the main factor impacting the final aspect ratio and thus identified the range of seed loading that would result in undesired powder flow. © 2015 American Institute of Chemical Engineers *AIChE J*, 61: 4456–4469, 2015

Keywords: habit, modeling, step propagation, crystallization

Introduction

The primary purpose of crystallization is purification based on liquid-solid phase separation, where the purified output is the solid phase. In industrial practice, crystallization processes are often designed around altering the solubility of the solid to ensure low final solubility to maximize the yield. In addition to chemical and physical purities, crystal size and habit are of paramount importance as they can strongly affect powder behavior in post-crystallization processing such as blending, granulation, tableting, and powder performance such as dissolution rate. The importance of crystal habit (and size) led to several theories with approximately chronological increasing levels of complexity. One of the earliest accounts about crystal habit prediction found in the literature is the monograph by Häuy[1] who predicted that crystals' faces would have simple intercepts with crystal axes that translates into the faces with the lowest indices being predominant in the equilibrium crystal shape. Wulf[2] and Gibbs[3] noted that equilibrium crystal shape would be that which corresponds to the minimum free energy. Later, Donnay and Harker[4] proposed that crystal internal structure must affect crystal habit. The theory they presented which came to be known as the Bravais, Friedel, Donnay and Harker (BFDH) law is based on the work on the geometry of crystals of Bravais[5] and on the triple periodicity and orientation of crystals of Friedel[6] and considers that individual face crystal growth is proportional to the inverse of the interplanar spacing. Few years after the introduction of the BFDH law, Hartman and Perdock[7–9] introduced the periodic bond chain (PBC) formalism to predict crystal habit. Their approach is also based on crystal internal structure but considers three different types of faces based on their locations with respect to PBC vectors, namely: kinked (K), stepped (S), and flat (F). Hartman and Perdock's theory takes into consideration the internal crystal structure and the energy involved in the attachment of crystallization units on the different types of faces and came to be known as the attachment energy (AE). Prediction of crystal habit via the BFDH and the AE theories are very useful tools in obtaining *ab initio* estimates of crystal habit based on crystal lattice data. However, these models need to be considered with caution as both theories do not include the effect of the media and environment of the growing crystals on crystal habit. It is an established fact that solvents, impurities, and additives can have a dramatic effect in modifying crystal habit (e.g., Meenan et al.[10]). In recent years, extensive development had been achieved in considering the effect of crystal environment on crystal growth and habit. In particular, researchers from Doherty's group[11–18] relied on the Burton, Cabrera and Frank (BCF) spiral growth theory (Burton et al.[19]) to develop a general framework for predicting crystal shape taking into consideration crystal growth media (i.e., solvent, additives, and imposters effects on crystal habit).

Although the theories stated above are very valuable and useful in obtaining a prediction of crystal habit, they have two main drawbacks for their application in industrial settings:

- They are based on the precise knowledge of the crystal structure, which often is not available unless large crystals can be obtained.

Correspondence concerning this article should be addressed to L. Derdour at lotfi.x.derdour@gsk.com

• They are often valid under conditions that are removed from industrial practice: no considerations of solvent/impurities/additive effects (BFDH and AE theories), low supersaturation (models based on BCF theory), no effect of mixing.

In recent years, several authors utilized an aspect ratio (or elongation factor) in order to describe crystal habit.[20–25] This approach requires the determination of only two characteristic sizes of a growing crystal. This approach was justified by the fact that in practice, two crystal dimensions are generally considered as sufficient to correlate with the resulting powder flowability and propensity for segregation which are the main powder properties of interest for the product end use. Using the aspect ratio as a habit descriptor presents the advantage of relatively straightforward experimental determination, typically via image analysis. It is evident that the aspect ratio approach has a drawback since it describes a three-dimensional (3-D) object with a two-dimensional (2-D) descriptor. In the literature, two approaches were used to address this issue:

• Assumption of symmetry in the third dimension (i.e., width equals to depth) as utilized by Borsos and Lakatos,[20] Sato et al.,[21] Briesen,[22] Gunawan et al.,[23] Ma and Wang,[24] and Ochsenbein et al.[25]

• Neglecting the growth in the third dimension because of negligible growth rate compared to the growth to the other two dimensions (e.g., Oullion et al.[26])

In cases where these two assumptions are not valid, the aspect ratio concept can lead to significant deviations from the actual shape as noted by Patience and Rawlings.[27] If applicable, the approach of modeling crystal shape via two characteristic crystal sizes offered simplicity in model derivation that allows including other phenomena such as nucleation, agglomeration, and breakage in the models for predicting crystal size and habit.

Approaches based on aspect ratio prediction are essentially semi-empirical in nature and require parameter refinement from experimental data. These approaches are usually based on the resolution of mass and heat balances along with population balance equations (PBEs). Accounts in the literature indicate that various phenomena depending on the systems at hand were considered and no single approach can be considered as universal. Puel et al.[28] proposed a 2-D PBE including nucleation and assuming size-independent growth rates. Subsequently, Puel et al.[29] extended their PBE system to include size-dependent growth rates through crystal size dependence upon diffusion. Matthews and Rawlings[30] presented a PBE-based model and a parameter estimation algorithm for size-independent crystal growth and variable crystal shape due to breakage (i.e., size-dependent contact secondary nucleation). They successfully utilized their model to optimize filtration. Briesen[22] introduced a model reduction based on crystal volume and a shape factor. This model considers a size-independent crystal growth and nucleation and is based on the resolution of a system of PBEs. Oullion et al.[26] presented a PBE-based model that considers a size-independent growth and includes secondary surface nucleation and contact nucleation to predict two characteristic lengths of a substance that crystallizes as a rectangular plate. Ma and Wang[24] proposed a morphological PBE solver scheme for a growth dominated process using empirical expressions for size-dependent growth rates. Ochsenbein et al.[25] approximated the fast growing face of columnar crystals to a circle and proposed a morphological PBE resolution algorithm for a size-dependent growth rate where two growth directions are considered with only one direction having a size-dependent growth rate. They utilized an empirical correlation for growth rate in for the direction with a size-independent growth and a semi-empirical equation derived from the birth and spread theory for the direction with size-dependent growth. Borchert and Sundmacher[31] presented a 2-D PBE resolution scheme for a growth dominated cooling crystallization utilizing empirical correlations for a size-independent growth and presented a framework for correlating 3-D crystal shape to corresponding 2-D projections. They also presented a growth parameters estimation algorithm and showed how the amount of experimental data can affect the estimation. Borsos and Lakatos[20] and Sato et al.[21] included crystal breakage in their 2-D PBE system. Shoji and Takiyama[32] presented a PBE including the effect of temperature, which allowed predicting appropriate modulated cooling to improve the aspect ratio.

In a previous study (Derdour et al.[33]), we presented a model for crystal growth for cubic crystals of constant habit. In the present work, we present a modification to the model to account for the variation of crystal shape during crystallization for crystals with parallelepipedic shape. The model presented herein is concerned with systems where crystal growth is the main phenomenon occurring during crystallization and where crystal habit can be characterized by two main characteristic dimensions (i.e., length and width). The model is based on Kossel's formalism[34] to derive expressions of growth rate in the two main directions of growth. Namely, growth rate is considered to occur via step propagation the velocity of which is face dependent. The approach applies to isothermal anti-solvent crystallizations operating at moderate supersaturation. We also present a parameter estimation algorithm to determine solute integration coefficients for crystal growth in two directions. The algorithm requires experimental data about temporal evolution of concentration (or supersaturation) and the aspect ratio at the end of the seed age and the final aspect. The data required is extracted from only few scale-down crystallization experiments that mimic commercial scale which represents a practical use in industrial settings. In this study, concentration during crystallization is determined via *in situ* and online Fourier Transform Infrared Reflectance (FTIR) spectrometry combined with an Attenuated Total Reflectance (ATR) probe and particles average aspect ratio is determined offline via microscopy. The model was found to describe reasonably well the crystallization behavior of a Bristol-Myers Squibb's investigational drug and hence could be utilized for predictive purpose as long as crystallization conditions result in crystal growth being the main occurring phenomenon.

Model Formulation

Kossel's formalism[34] for crystal growth mechanisms considers that crystals are faceted and grow via step propagation on each face. The model presented herein is based on the one-step-per-face simplification reported previously[33] and briefly described below.

The steps are created by surface nucleation and/or surface defects and dislocations that increase with supersaturation as reported by Myerson and Ginde.[35] However, for systems operating at moderate supersaturations, the density of kinks and defects on the crystal surface and the probability for conditions of rough surface growth (i.e., simultaneous surface nucleation events) can be considered low. In addition, under these conditions, the propensity for step bunching is low as

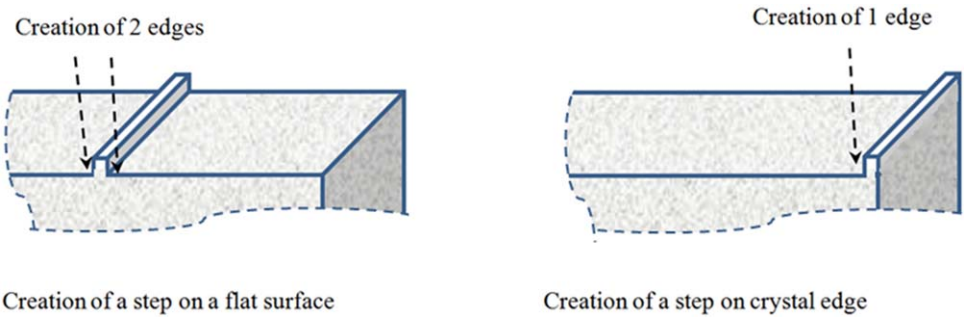

Figure 1. Comparison between a step formation on a flat surface and on face's edge.

[Color figure can be viewed in the online issue, which is available at wileyonlinelibrary.com.]

noted by Chernov and Komatsu.[36] Moreover, under conditions of moderate supersaturation, new steps are created via surface nucleation preferentially at the surface edges once the step has finished covering the whole face as reported by Mullin[37] and Kossel.[34] This behavior is consequent to the surface energy (reported per unit area) minimization principle: the addition of a step on a flat surface results in an additional kink (cf. Figure 1) that results in more unbalanced molecular forces compared to the addition of a step on the edge of a face which results in the creation of only one kink. Therefore, the resulting increase in surface energy per unit area is expected to be higher if a new step is created on a flat surface as island compared to the edge of a face. Additionally, as the growing crystal has a tendency to minimize its surface energy (reported per unit area), as long as there is a step propagating on a crystal face, growth units will preferably dock at that moving step rather than create a new step. As a consequence new steps are created once the step had finished forming an additional layer of molecules. Based on the considerations above and for systems operating at moderate supersaturations, we utilize a one-step-per-face approximation were we consider that a new step is created by surface nucleation at the face's edge after completion of the previous step. This approximation is analogous to the expected equivalent behavior between faces containing many dislocations and other same faces containing only one dislocation for the BCF mechanism as reported by Mullin.[37]

The other main assumptions of the following formulation are:

- Surface integration is the limiting step of crystal growth kinetics (i.e., no diffusion limitations).
- Concentration is uniform in the crystallizer.

Linear growth rate in a given direction is directly related the step advance velocity of the adjacent face. For growth dominated processes, Bennema and Gilmer[38] established the following relationship for the step propagation velocity

$$v_{sa} = \left[\left(V_m L_m^2/\lambda_0\right)\upsilon e^{\left(-\frac{E_a}{RT}\right)}\right](C_{int} - C^*) \tag{1}$$

In this expression, V_m is the solute molecular volume and L_m is the molecular length. The activation energy for surface integration (E_a) as well as the distance between kink (λ_o) can be face dependent, which translates into different step advance velocities on different faces and different face linear growth rates.[38,39]

In the following formulation, parallelepipedic crystal shape is considered and the growth of each face occurs via the propagation of a step parallel to the adjacent face. Crystal symmetry is assumed where the width of the crystal is equal to its depth as shown in Figure 2. We define the two main characteristic sizes of a growing crystal, namely, the length (L) of the slow growing faces noted $\mathcal{L}$ and the width (W) of the fast growing faces noted $\mathcal{W}$. Knowing that for systems where the integration step is the limiting step, the solute concentration at the interface film/surface can be approximated to the bulk solute concentration (Garside et al.[40]), we can write the expressions of the step advance velocity on each faces and Eq. 1 can be simplified for steps propagating on faces $\mathcal{L}$ and faces $\mathcal{W}$ as follows

$$v_{saL} = \alpha_L S \tag{2}$$

and

$$v_{saW} = \alpha_W S \tag{3}$$

where α represents the factor in square brackets in Eq. 1 and S is the absolute supersaturation

$$S = C - C^* \tag{4}$$

where C is the concentration of the solute in the crystallizer and C^* is the solubility which in this study is expressed by a polynomial relationship

$$C^* = \sum_{i=1}^{5} a_i x_{AS}^i \tag{5}$$

where x_{AS} is the mass fraction of the anti-solvent in the solvent system.

In the following formulation, the initial crystal size corresponds to the seed size which is classified in N_c number of classes of particles, each having the same size. For the case of a parallelepipedic shape (cf. Figure 2), one can write the equations related to the addition of consecutive layers of solute molecules on the crystal surface of class i and the consecutive durations to add a complete layer. The increase of the length of faces $\mathcal{L}$ of crystal of class i ($1 \le i \le Nc$) is a result of the growth of faces $\mathcal{W}$. The completion of two layers of growth

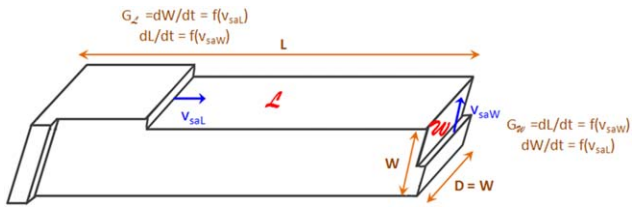

Figure 2. Crystals with two characteristics faces and propagating steps on each face.

[Color figure can be viewed in the online issue, which is available at wileyonlinelibrary.com.]

units on faces $\mathcal{W}$ results in the following increase in the length of face L

$$L_i(t_h) - L_i(t_{h-1}) = 2\sigma_s \tag{6}$$

where σ_s is the step thickness assumed to be constant in both faces.

The time needed to complete one layer coverage on face $\mathcal{W}$ that results in an increase of $2\sigma_s$ in length (L) can be expressed by

$$\Delta t = t_h - t_{h-1} = \frac{W_i}{v_{saW}} \tag{7}$$

The time required for a step to cover a face and the step thickness can be considered as very small.[33] Hence Eqs. 6 and 7 can be combined to yield

$$\frac{dL_i}{dt} = \frac{2\sigma_s v_{saW}}{W_i} \tag{8}$$

Substitution of Eq. 3 in Eq. 8 yields the expression of the growth rate of face $\mathcal{W}$ of crystals of class i

$$(G_{\mathcal{W}})_i = \frac{dL_i}{dt} = \frac{k_W S}{W_i} \tag{9}$$

where k_W is defined as the solute integration coefficient of faces $\mathcal{W}$ (i.e., fast-growing faces)

$$k_W = 2\sigma_s \alpha_W \tag{10}$$

k_W can be assumed constant for a given face if the distance between kinks (λ_o) is constant.

Similar reasoning applies to the increase of the thickness of crystals of class i. The resulting equation relating crystal growth rate of face $\mathcal{L}$ can be found to be

$$(G_{\mathcal{L}})_i = \frac{dW_i}{dt} = \frac{k_L S}{L_i} \tag{11}$$

Similarly, k_L is defined as the solute integration coefficient of faces $\mathcal{L}$ (i.e., slow-growing faces)

$$k_L = 2\sigma_s \alpha_L \tag{12}$$

Combination of Eqs. 9 and 11 yields

$$\frac{dL_i}{L_i} = \frac{k_W}{k_L}\frac{dW_i}{W_i} \tag{13}$$

Integration of Eq. 13 between the limits L_{i0} to L_i and W_{i0} to W_i provides the relationship between the length and the width of crystals of class i

$$L_i = A\ W_i^{k_e} \tag{14}$$

where

$$A = \frac{L_{i0}}{W_{i0}^{k_W/k_L}} \tag{15}$$

and

$$k_e = k_W / k_L \tag{16}$$

Substitution of Eq. 14 in Eq. 9 yields the expression for the width during crystallization

$$W_i(t) = \left[W_{i0}^{k_e+1} + (k_W + k_L) A^{-1} \int_0^t S(t)dt \right]^{1/(k_e+1)} \tag{17}$$

For growth dominated processes assuming symmetry in the third direction (i.e., width = depth) and knowing that crystals' length and width and related via Eq. 14, one can write the general expression for the mass of solute crystallized at time t as

$$m_{cr} = \rho_{cr} \Psi \int_{W_{min}}^{W_{max}} d\ \left[\left(AW^{\ 2+k_e} - L_0 W_0^2 \right) n(W) \right] \tag{18}$$

where Ψ is a correction factor to account for non-right angles between the sides of parallelepipedic crystals (see Appendix for the definition of Ψ); $n(W)$ is the number based density of crystal width, W_{min} and W_{max} are respectively the minimum and the maximum of the crystal width distribution at time t.

Introducing Eq. 18 in product mass balance yields the expression of the transient concentration during crystallization

$$C(t) = \frac{m_0 - \rho_{cr} \Psi \int_{W_{min}}^{W_{max}} d\left[\left(AW^{2+k_e} - L_0 W_0^2 \right) n(W) \right]}{M w_{slt} \left((V_{solv})_0 + AR\ \ m_0 t \right)} \tag{19}$$

where AR is the anti-solvent addition rate defined as

$$AR = (V_{AS}/t_{AS})/m_0 \tag{20}$$

In the following approach, the initial particle size distribution (PSD) is discretized into Nc classes. The number of crystals in each class is kept constant during crystallization and the sizes of crystals in each class increase during the operation. Hence $n(W)$ is independent of W. Introducing the PSD discretization, Eq. 18 can be transformed to its discretized counterpart as follows

$$m_{solute} = m_0 - \rho_{cr} \Psi \sum_{i=1}^{Nc} N_i \left(L_i W_i^2 - L_{i0} W_{i0}^2 \right) \tag{21}$$

where N_i is the number of crystals in class i.

Consequently, Eq. 19 can be simplified to its discretized form as

$$C(t) = \frac{m_0 - \rho_{cr} \Psi \sum_{i=1}^{Nc} N_i \left(L_i W_i^2 - L_{i0} W_{i0}^2 \right)}{M w_{slt} \left((V_{solv})_0 + AR m_0 t \right)} \tag{22}$$

Resolution of Eqs. 9, 11, 14, 17, and 22 requires the estimation of growth parameters k_L and k_W. In the following section, we present an estimation algorithm to determine these parameters from few experimental data of temporal evolution of concentration and aspect ratio at the end of the seed age and the final aspect ratio. Once determined, the solute integration coefficients is utilized for simulation and prediction purposes.

The algorithm was applied for the crystallization of an investigational compound at Bristol-Myers Squibb Co., which will be referred to as compound X for the sake of confidentiality. This substance crystallizes in the parallelepipedic shape with a habit that can be characterized by an aspect ratio, length/width. In the experimental section, we present examples of parameters estimation and comparisons between the model predictions and experimental data.

Materials and Methods

Crystallization experiments were carried out in an experimental set-up depicted on Figure 3. It consists of a jacketed 200-mL reactor, equipped with an overhead stirrer, Chemglass, IP42,

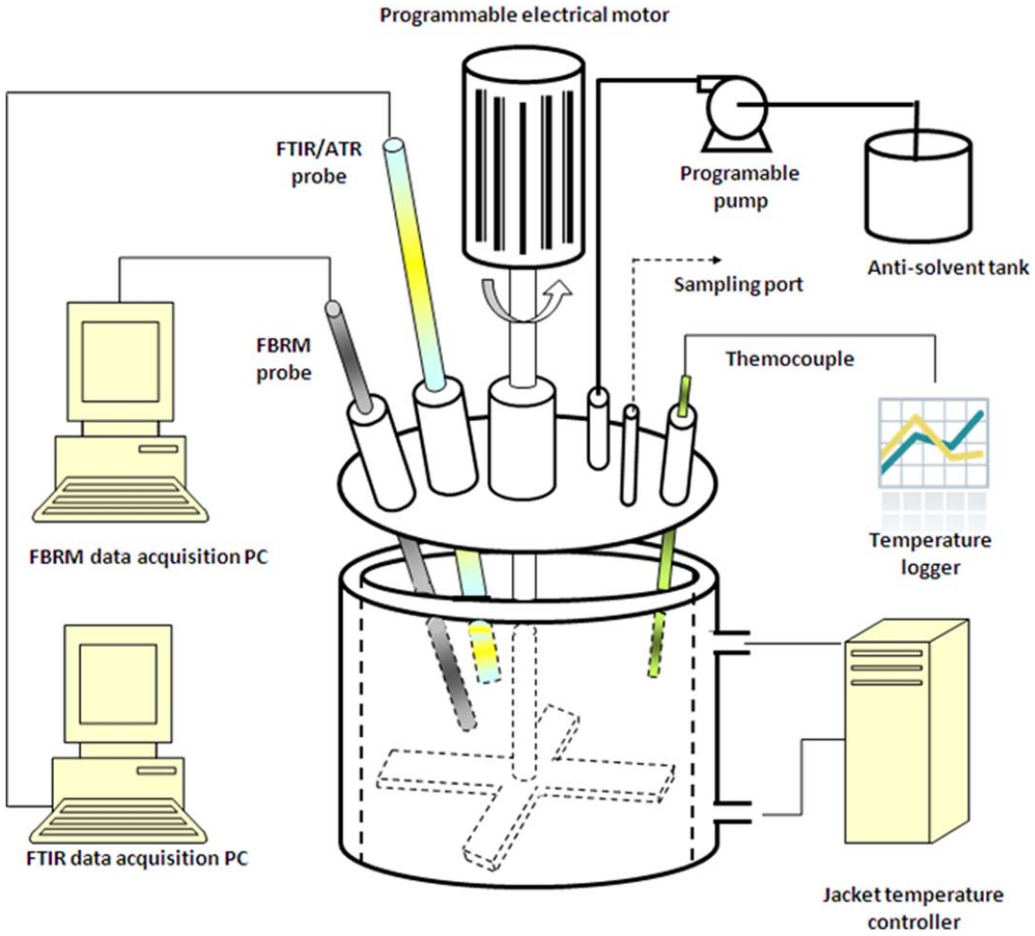

Figure 3. Experimental set up.

[Color figure can be viewed in the online issue, which is available at wileyonlinelibrary.com.]

range: 50–2000 rotations per minute (RPM), and a four-pitch-blade agitator. Temperature was controlled by an external circulator (Thermo Electron Corporation, Model Haake Phoenix II P2), using glycol/water as the heat transfer fluid. Mixture temperature was monitored continuously using a thermocouple connected to a digital data logger. The anti-solvent was added via a dosing pump (Stepdos RC, KNF Flodos AG, Sursee, Switzerland). Concentration during crystallization was measured on line via *in situ* ATR immersion probe connected to an infrared spectrometer (ReactIR^{TM}4000 Mettler-Toledo, OH).

Bristol-Myers Squibb Compound X was obtained in house with purity higher than 99% by high performance liquid chromatography (HPLC) analysis. Solvents were obtained from J. T. Baker and were all of HPLC grade. Crystallization was carried out according to the following procedure, the compound was dissolved in Methanol at 50 C. A first portion of Acetone which acts as the anti-solvent was then added in 5 min to create supersaturation. Seeds were then introduced in the reactor and the suspension was aged for 2 h. A second portion of Acetone was then added at a given constant rate for each experiment. The slurry was then cooled down to 20°C in 1 h and filtered. The wet cake was washed twice with 2 volumes of acetone and then dried under vacuum for about 6 h at 50°C. There was practically no solute present in the final solvent system, resulting in no risk of precipitation during the cake wash. Particle size distribution was determined by laser light scattering analyzer (Mastersizer 2000, Malvern Instruments, Worcestershire, UK) equipped with a wet cell. Isopropyl alcohol saturated with compound X as dispersant and no sonication was employed during the measurements. Scanning electron microscopy (SEM) images were obtained with a SEM microscope (XL30 ESEM ODP, FEI company, Hillsboro, OR).

The seeds PSD in numbers was classified into 20 classes of sizes. As only crystal growth is considered, the number of particles in each size class is maintained constant during

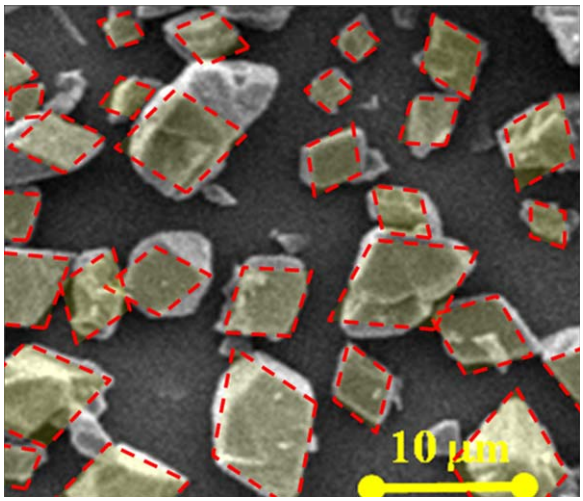

Figure 4. Microscopy image of seeds.

[Color figure can be viewed in the online issue, which is available at wileyonlinelibrary.com.]

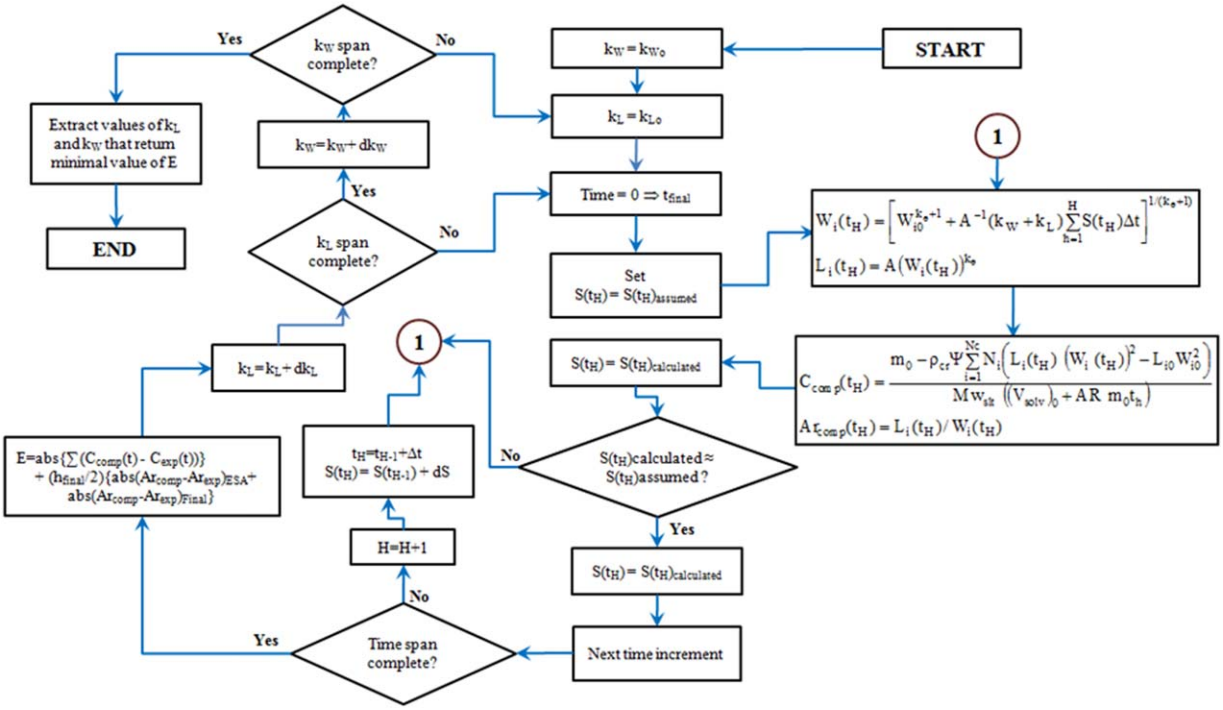

Figure 5. Parameter estimation algorithm.

[Color figure can be viewed in the online issue, which is available at wileyonlinelibrary.com.]

crystallization and growth of the crystals in each class is computed. The seeds were obtained by jet-milling parent material and based on SEM image shown in Figure 4, their shape can be approximated as parallelepipedic with non-right angles between faces and equal sides ($(L_{i0})_{seeds} = (W_{i0})_{seeds}$). The milling step creates some surface defects on the surface of the seeds which heal rapidly during the seed age period. The seeds had a median unweighted size (d50) of 6.4 μm. The PSD of the seeds and SEM images at the end of the seed age are reported in the results and discussion section.

Measurement of the aspect ratio

In this study, the experimental crystals' aspect ratio at the end of the seed age and the final aspect ratio were determined using the following procedure: At the end of the seed age and at the end of crystallization, 2 mL of the suspension was rapidly filtered at room temperature using a centrifuge with a spinning rate set at 10,000 RPM for 30 s (Centrifuge 5417C, Eppendorf, Hauppauge, NY). Crystals were transferred from the centrifuge filters to microscope slides via gentle tapping the outside of the filters to minimize crystal breakage. Average

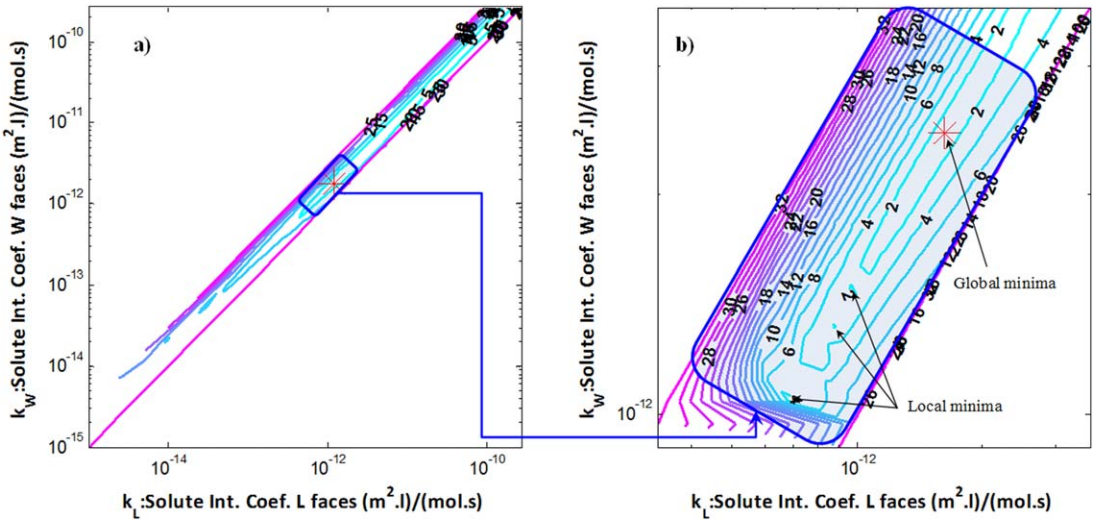

Figure 6. Two-tier parameter estimation. Plot of total error vs. k_W and k_L.

(a) Low-resolution scan of entire range of values of k_W and k_L; (b) high-resolution scan in area of location of global minima of the total error. [Color figure can be viewed in the online issue, which is available at wileyonlinelibrary.com.]

Table 1. Experimental Conditions Used for Parameter Estimation

Exp. #	*SL* (% Input)	*AR* (mL/(min g)	*So* (mol/L)
1	2	0.153	0.053
2	1	0.157	0.041
3	1	0.067	0.041
4	2	0.103	0.050
5	2	0.153	0.053
6	1	0.150	0.100

Table 2. Aspect Ratios and Maximum Supersaturation Reached During the Anti-Solvent Addition Period for the Experiments Used for the Parameter Estimation

Exp. #	1	2	3	4	5	6
Ar_{SA} (–)	1.61	1.64	1.35	1.54	1.63	1.76
Ar_{ASA} (–)	1.88	1.94	1.52	1.64	1.89	1.92
S_{max_ASA} (mol/L)	0.0246	0.0351	0.0293	0.0245	0.0252	0.0149

crystal size length and width were measured off line using optical microscopy (Zeiss Axio scope. A1, Carl Zeiss Microscopy, LLC, Peabody, MA). This measurement technique can present the disadvantage of crystals preferential orientation resulting in the measurement being biased toward the large faces. However, this effect was considered negligible given the symmetry of the crystals. For each sample, the analysis was performed on a population of about 600 individuals which is typically considered as sufficient for obtaining an acceptable representative analysis.[28,41,42]

Parameter estimation algorithm

The parameter estimation algorithm is based on the minimization of the total error between computed and experimental concentration during crystallization and aspect ratios at the end of the seed age and the end of crystallization. The objective function is defined as

$$E=\sum_{h=1}^{h_{\text{final}}} \text{abs}[C_{\text{comp}}(t_h)-C_{\text{exp}}(t_h)]+({}^{h_{\text{final}}}/_{2})\,abs[Ar_{\text{comp}}(t_{h_{\text{final}}})-Ar_{\text{exp}}(t_{h_{\text{final}}})] \tag{23}$$

where h_{final} corresponds to the total number of experimental acquisition points for solute concentration.

There is a much larger number of experimental data acquisition about concentration (h_{final} in the range of 80 to 300 data point) compared to experimental data about the aspect ratio (only two data points). The term ${}^{h_{\text{final}}}/_{2}$ is included in the objective function to avoid parameter estimation bias toward minimizing the error on the computation of concentration which can result in a poor estimation of the aspect ratio. The principle of the method is based on extracting the values of k_L and k_W that provide the lowest total error. Several approaches for parameter estimation were envisaged. Simplex refinement methods were initially investigated. However, it was found that these methods can extract values of k_L and k_W that correspond to local minima of the total error. This shortcoming is possibly due to the inherent local and sequential scanning basis of the simplex methods.

Next, we investigated writing an algorithm that would scan the entire range of possible values of k_L and k_W to extract their values corresponding to the global minima of the total error. Because high resolution estimation is required, this algorithm execution turned out to be very time consuming. In order to improve the algorithm by shortening its execution time while maintaining a high resolution estimation, two features were added to it:

- As k_L is always lower than k_W, we limited the scan of k_L to lower values of k_W. In addition, we limit the lowest value of k_L to $k_W/3$ because based on Eqs. 14 and 15 the estimated aspect ratio becomes unrealistically high for ratios $k_W/k_L > 3$.
- Utilize a two tiers estimation algorithm: At first utilize a low resolution estimation to pinpoint the area of the global minima. Then scan the area of the global minima with a high resolution in order to extract the values of k_L and k_W.

These modifications resulted in major improvement of the parameter estimation algorithm with execution times shortened from several hours to about 5–20 min depending on the length of the experiment utilized for the estimation. The flow chart of the parameter estimation algorithm is shown in Figure 5 and an example of the variation of the total error with the solute integration coefficients and localization of the global minima of the total error is shown in Figure 6.

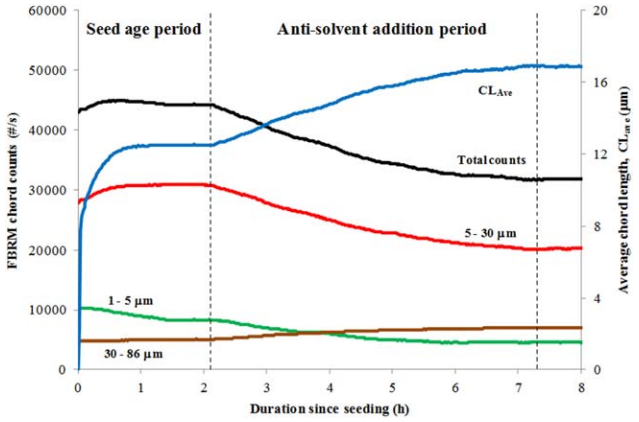

Figure 7. Typical evolution of FBRM counts during growth-dominated crystallization.

[Color figure can be viewed in the online issue, which is available at wileyonlinelibrary.com.]

Results and Discussion

Parameter estimation

Table 1 summarizes the crystallization conditions of the experiments utilized to estimate the solute integration coefficients of k_L and k_W where the seed loading is defined as

$$SL=100\ \frac{m_{\text{seeds}}}{m_0} \tag{24}$$

The ranges for the initial supersaturation (*So*) and the anti-solvent addition rate (*AR*) were selected so as to keep the total duration of crystallization below 8 h and to ensure that the relative supersaturation does not exceed 200%, which focused beam reflectance measurement (FBRM) indicated increase of fine counts and fooling of the probe that indicates nucleation becomes non-negligible. The relative supersaturation is defined as

$$RSS=100\ (C-C^*)/C^* \tag{25}$$

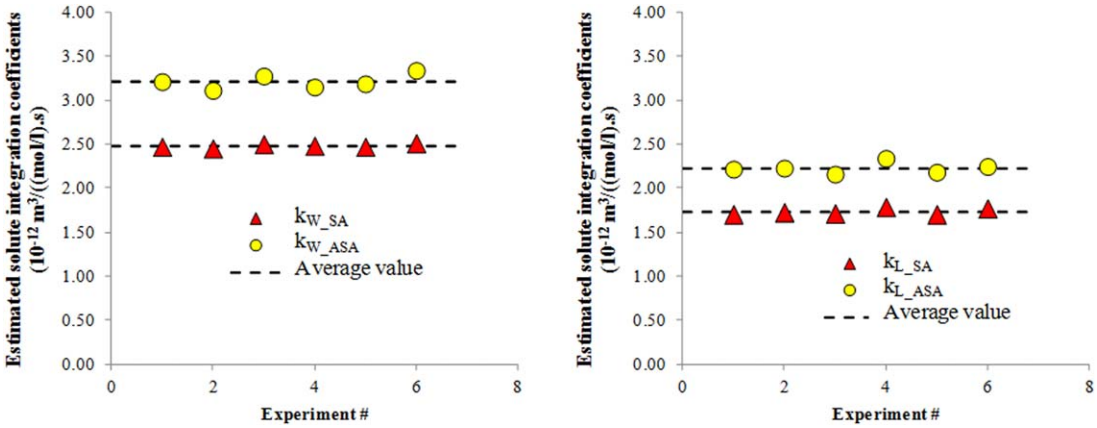

Figure 8. Estimated k_L and k_W.

[Color figure can be viewed in the online issue, which is available at wileyonlinelibrary.com.]

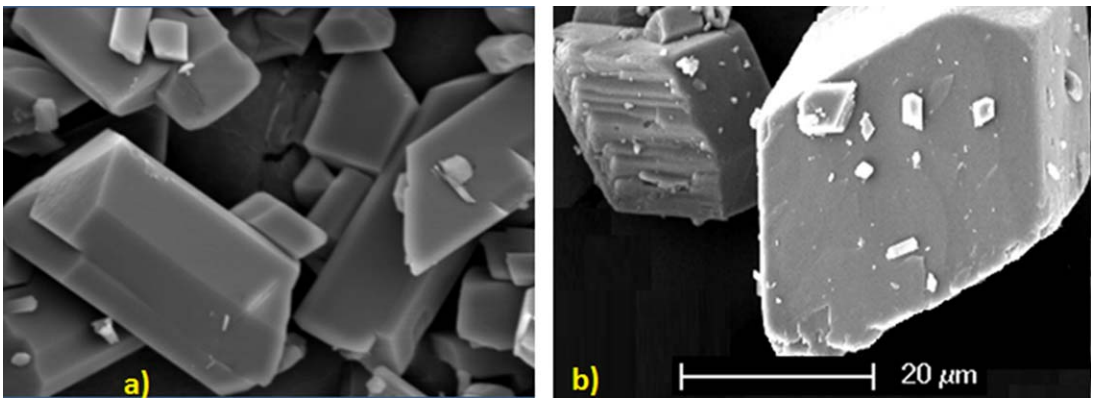

Figure 9. Typical SEM images of crystals; (a) at the end of the seed age and (b) final crystals.

[Color figure can be viewed in the online issue, which is available at wileyonlinelibrary.com.]

An example of FBRM data indicating growth dominated crystallization occurring when the relative supersaturation is below 200% is shown in Figure 7. The decrease in total number of chord counts during the anti-solvent addition period has been correlated to the effect of dilution. The aspect ratios obtained at the end of the seed age period, the final aspect ratios, and the maximum supersaturation reached during the anti-solvent addition period are shown in Table 2. The parameter estimation results are shown in Figure 8 which indicates that k_L and k_W obtained during the anti-solvent addition period are slightly larger than the values obtained during the seed age period.

During the anti-solvent addition period, crystal size is significantly larger that the size during the seed age. The observed higher solute integration coefficients during the anti-solvent addition period can be explained by the effect of larger crystals on crystal growth rate.

- It is generally accepted that as crystal size increases, the crystal strain becomes more pronounced, which can result in increased surface dislocations and defects. This results in an increase of the solute integration coefficient (Garside and Davey[43]).
- Large crystals have larger kinetic energy than smaller crystals and deviate from fluid streamlines more readily (Garside et al.[40]). Hence they collide with each other and with reactor parts more often than smaller crystals. In addition, the energy involved in the collisions increases with crystal size. These collisions can create surface defects which become additional growth sites and hence contribute to the increase of the solute integration coefficients. Conversely, collisions can also create crystal fragments that contribute in decreasing the overall growth rate since breakage is not considered. However, based on FBRM data, which does not show an increase in total number of counts, we consider that the effect of the creation of crystal fragment on the measured growth rate is negligible. Nevertheless, we believe that the solute integration coefficient obtained during the anti-solvent addition period is likely to reflect some level of crystal breakage and increased growth rate due to higher density

Table 3. Experimental Conditions Used for Computation and Model Validation

Exp. #	*SL* (% of Input)	*AR* (mL/(min g)	*So* (mol/L)
7	1	0.03	0.011
8	1	0.07	0.030
9	2	0.1	0.049
10	0.75	0.04	0.098
11	0.75	0.04	0.055
12	0.75	0.15	0.060
13	2	0.15	0.061
14	2	0.04	0.060

of surface defects. The presence of surface defects and small number of fines is evidenced in Figure 9, which shows SEMs of crystals isolated at the end of the seed age and final crystals.

On the other hand, the data in Figure 8 shows that the solute integration coefficients are approximately constant in each period (seed age or anti-solvent addition) regardless of the experiment conditions. This result indicates that the solute

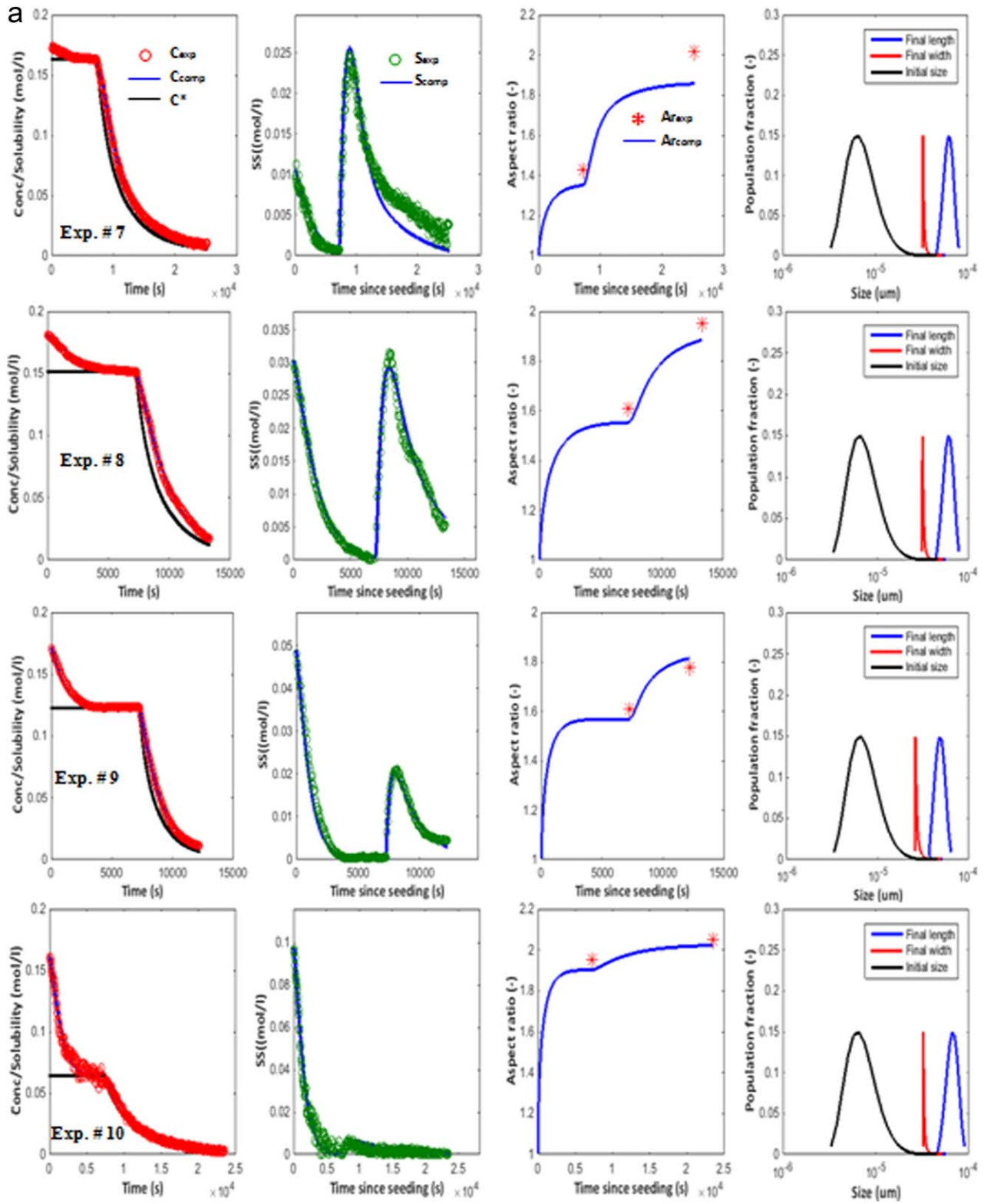

Figure 10. Comparison between computed and experimental data.

[Color figure can be viewed in the online issue, which is available at wileyonlinelibrary.com.]

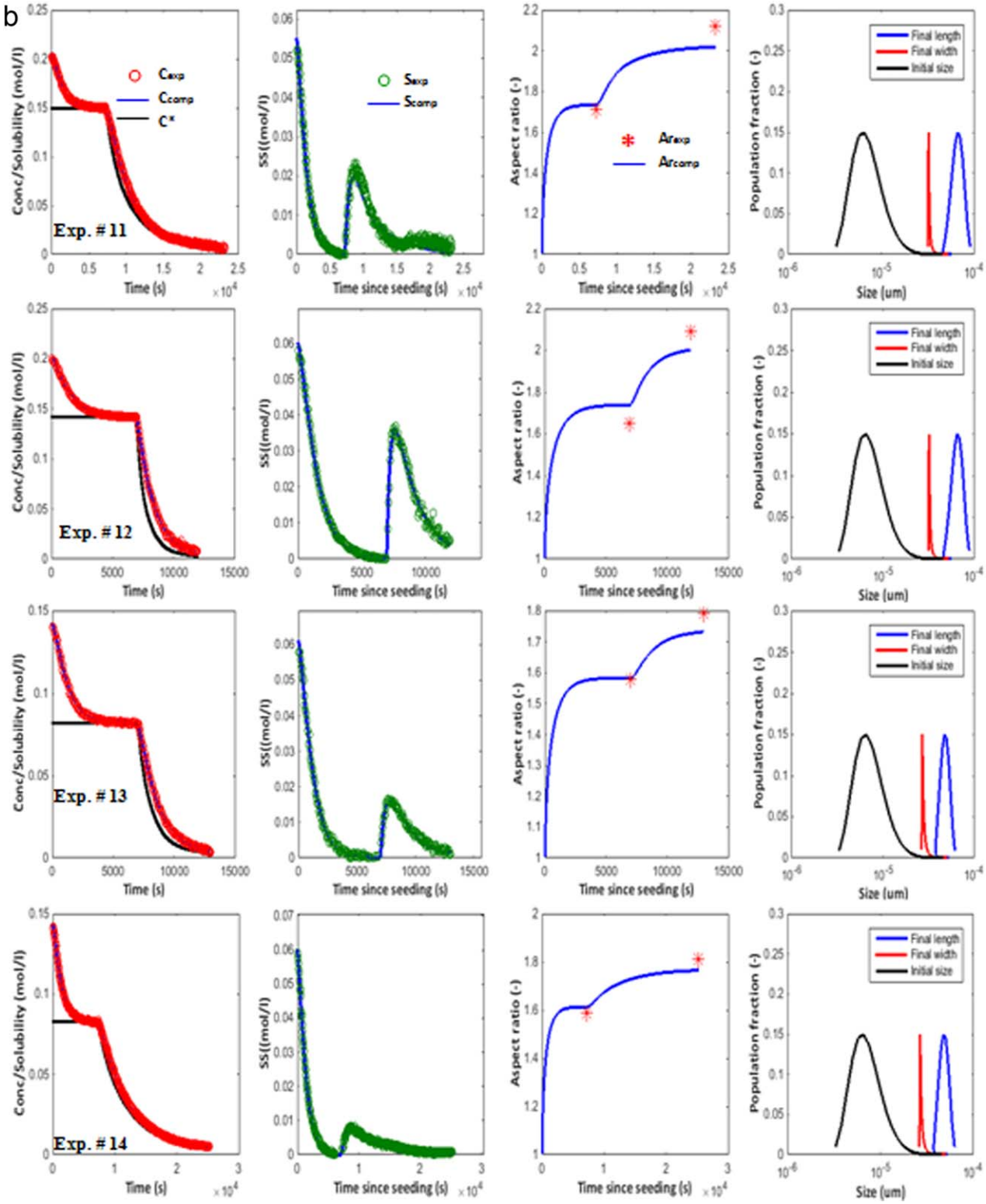

Figure 10. Continued

integration coefficients can be considered as independent of crystallization conditions in each period and within the process parameters ranges explored. In the following section, the average experimental values of k_L and k_W will be utilized for the prediction of concentration, supersaturation, and aspect ratio and comparison with experimental data and for process simulation.

Model's predictions

The average estimated values of k_L and k_W are used in the resolution of Eqs. 9, 11, 14, 17, and 22, which were solved numerically for any given set of experimental conditions to provide the variation of concentration, the absolute

Table 4. Statistical Analysis of Computation

	R^2 for Prediction of C and SS				Relative Error on Prediction of *Ar* (%)					
					At End of Seed Age			Final		
	Seed Age Period		Anti-Solvent Addition Period		*Ar* Values (–)			*Ar* Values (–)		
Exp. #	C	SS	C	SS	Exp.	Computed	Rel. Error	Exp.	Computed	Rel. Error
7	0.952	0.952	0.997	0.869	1.43	1.39	2.79	2.02	1.89	6.38
8	0.995	0.996	0.998	0.919	1.61	1.55	3.52	1.95	1.89	3.29
9	0.984	0.985	0.999	0.965	1.61	1.58	2.15	1.78	1.82	2.39
10	0.974	0.987	0.989	*0.115*	1.95	1.91	2.18	2.05	2.03	1.07
11	0.998	0.998	0.998	0.877	1.71	1.75	2.10	2.12	2.03	4.14
12	0.999	0.999	0.999	0.922	1.65	1.74	5.58	2.09	2.01	3.99
13	0.993	0.994	0.999	0.959	1.58	1.60	1.26	1.79	1.75	2.17
14	0.998	0.999	1.000	0.979	1.59	1.62	1.84	1.81	1.77	2.11

supersaturation, and the aspect ratio during crystallization. Table 3 provides the experimental conditions used.

A comparison between experimental data and computation is shown in Figure 10a, b, and a statistical analysis of the computation is summarized in Table 4. The coefficients of determination indicate that the model provides a good prediction of the solute concentration and absolute supersaturation for most conditions investigated. Values of R^2 for the prediction of S during the anti-solvent addition period for Exp. # 10 are very low. In that run, the value of S remains very low and close to zero throughout the period in question. In this case, the coefficient of determination is not a good descriptor of correlations between predicted and actual values. Nevertheless, for Exp. #10, Figure 10a indicates a good prediction of the model.

Comparison between the aspect ratio defined as L/W, obtained experimentally at the end of the seed age and the end of crystallization with the predicted values are also shown in Table 3. The results show that the model predicts reasonably well the aspect ratio with a relative error of about 6.5%, which indicates an acceptable prediction. The good fit between experimental data and model's predictions also indicates that for this type of system, solute integration is the limiting mechanism throughout crystallization.

Process simulation

In order to experimentally determine the effect of the aspect ratio on powder flow, the flowability of different API lots were tested using the Carr index method defined as (Carr[44])

$$\mathrm{Carr}_{\mathrm{index}} = 100\left[\frac{(\rho_p)_{\mathrm{Tapped}} - (\rho_p)_{\mathrm{Bulk}}}{(\rho_p)_{\mathrm{Tapped}}}\right] \tag{26}$$

where $(\rho_p)_{\mathrm{Tapped}}$ is the powder's tapped density and $(\rho_p)_{\mathrm{Bulk}}$ is the powder's bulk density.

Experimental results are shown in Figure 11, which shows a plot of experimental Carr index vs. the average final aspect ratio of the corresponding powder. Knowing that values of Carr index lower than 20 are generally correlated with acceptable powder flowability,[44,45] it was considered that powders with aspect ratio above 2 represent a higher risk for issues related to powder flow during drug product manufacturing as they resulted in Carr indexes higher than 20. In order to determine crystallization conditions that lead to solids with aspect ratios lower than 2, we utilized the model to compute the evolution of the aspect ratio during crystallization and the final aspect ratio. Simulations were performed utilizing the same seed PSD and the predicted curves of the evolution of aspect

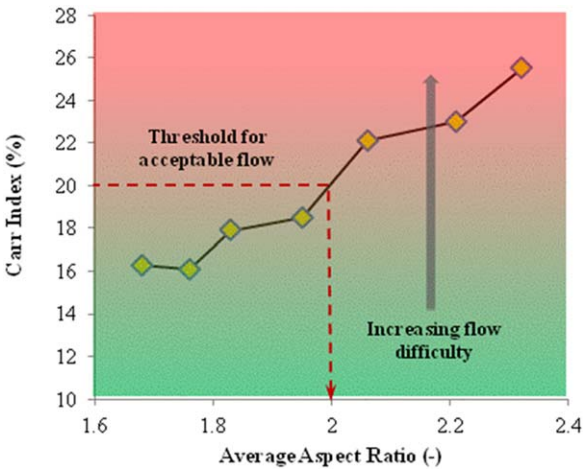

Figure 11. Variation of Carr index with final powder aspect ratio.

[Color figure can be viewed in the online issue, which is available at wileyonlinelibrary.com.]

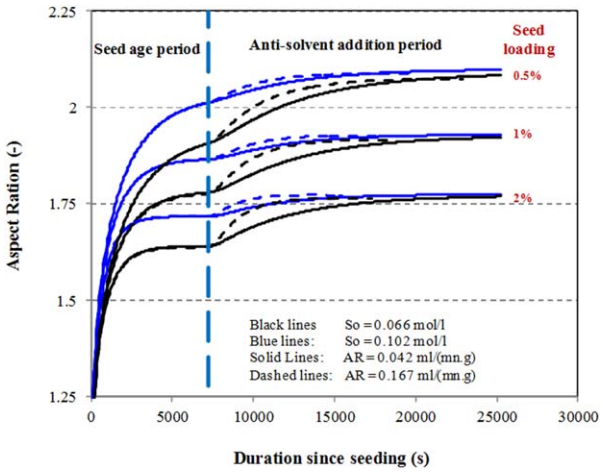

Figure 12. Predicted evolution of the aspect ratio during crystallization.

[Color figure can be viewed in the online issue, which is available at wileyonlinelibrary.com.]

Table 5. Crystallization Conditions Utilized in Simulation

SL (% Input)	0.5				1				2			
AR (mL/(min g)	0.04		0.17		0.04		0.17		0.04		0.17	
So (mol/L)	0.07	0.10	0.07	0.10	0.07	0.10	0.07	0.10	0.07	0.10	0.07	0.10

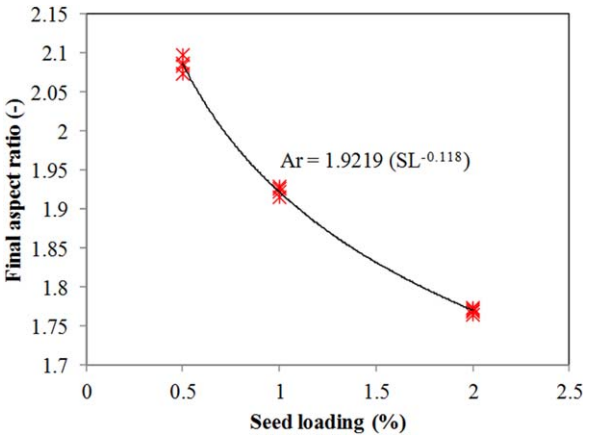

Figure 13. Variation of the predicted final aspect with seed loading.

[Color figure can be viewed in the online issue, which is available at wileyonlinelibrary.com.]

ratio during crystallization are shown in Figure 12. Table 5 summarizes the crystallization conditions that are part of the possible design space of crystallization and which were used for the simulation.

The results of the simulation shown in Figure 12 indicate that the final aspect ratio is mostly impacted by the seed loading within the ranges of parameters explored. Supersaturation during crystallization affects the evolution of the aspect ratio throughout the process but not its final value. The effect of seed loading on the final aspect ratio is likely a reflection of the final crystal sizes (L and W). For low seed loading, single seed crystals grow to larger sizes compared to larger seed loading. The more the crystal grows the higher the difference between the final length and width is obtained. This translates into larger aspect ratios obtained for lower seed loadings. The variation of the final aspect ratio with the seed loading is shown in Figure 13. The correlation extracted from Figure 13 indicates that seed loading higher than 0.75% are likely to result in final aspect ratios lower than 2, which in turn would result in low risk for issue related to powder flow during drug product manufacturing. The actual seed loading selected for the design space for this substance was between 0.8% and 1.5% and resulted in good powder flow during drug product formulation, in agreement with the model predictions.

Conclusion

A model for crystal growth in two directions is presented. The approach assumes the surface integration step as the limiting mechanism and computes crystal growth, supersaturation, and aspect ratio. The resolution requires the knowledge of solute integration coefficients on the two main crystal faces, namely, fast growing and slow growing faces. A parameter estimation algorithm was derived to determine those coefficients from experimental data about temporal variation of concentration during crystallization, final aspect ratio, and aspect ratio at the end of the seed age period. Estimated values indicated that the solute integration coefficient for large crystals is likely to be higher than values obtained for small crystals possibly due to higher density of defects expected on large crystals. Model computations were in good agreement with experimental data indicating a good prediction of the model. Model simulation showed that for a given seed size, the seed loading is the main factor affecting the final aspect ratio for the system at hand. Growth rates in both directions are different because of different surface integration coefficients resulting in different evolutions of length and width during crystallization. However, for the same seed loading, both profiles lead to the same final aspect ratio regardless of other crystallization parameters. The computation also allowed identifying the seed load range that would result in acceptable flow properties.

Acknowledgments

The authors are deeply thankful to Dr. D. B. Patience for valuable scientific discussions. The Leadership Teams at GlaxoSmithKline and Bristol-Myers Squibb Co. are kindly acknowledged for providing means that made this study possible.

Notation

Roman symbols

A = constant (Eq. 14) (–)
ai = coefficients (Eq. 5)
AR = anti-solvent addition rate (m^3/(kg.s)
Ar = aspect ratio (–)
C = concentration (mol/L)
C^* = solubility (mol/L)
Cl_{ave} = average chord length (μm)
d50 = median unweighted size (Sphere-equivalent diameter at 50% of the population of crystals) (μm)
E^+ = activation energy (J/mol)
k_w, k_L = solute integration coefficients (m^2/(mol/L).s)
k_e = ratio of solute integration coefficients (–)
L = size of slow growing faces or length (m)
$\mathcal{L}$ = denotes slow growing faces (–)
L_{io} = initial crystal length (m)
L_m = molecular size of crystallizing species (m)
m = mass (kg)
Mw_{slt} = molecular weight of solute (kg/kmol)
n = population number density function (–)
Nc = number of classes of crystals (–)
Ni = number of crystals of class i (–)
R = universal constant of gases (J/(mol K)
RSS = relative supersaturation (%)
S = absolute supersaturation (mol/L)
So = absolute supersaturation at seeding (initial supersaturation) (mol/L)

T = temperature (°C, K)
t = time (s, min, h)
t_{AS} = duration of anti-solvent addition period (s, min, h)
v_{sa} = step advance velocity (m/s)
V_{solv} = volume of solvent (m^3)
V_{AS} = volume of anti-solvent (m^3)
V_m = molecular volume (m^3/mol)
W = size of fast growing faces or width (m)
$\mathscr{W}$ = denotes fast growing faces (–)
W_{io} = initial crystal width (m)
x_{AS} = mass fraction of anti-solvent in solvent system (–)

Greek letters

α = constant (ms^{-1}/(mol m^{-3}))
λ_o = distance between kinks (m)
υ = molecular vibrational frequency (s^{-1})
ρ = density (kg/m^3)

Subscripts

ASA = refers to the anti-solvent addition period
bulk = refers to bulk powder
comp = computed value
cr = relates to crystal
exp = experimental value
final = final value
h, H = indices for discretized time (–)
i = refers to crystals of class i (–)
int = relates to the interface crystal face/liquid
min = minimum value
max = maximum value
0 = initial value
p = refers to powder
SA = refers to the seed age period
seeds = relates to seeds
solute = relates to solute
tapped = refers to tapped powder

Literature Cited

1. Häuy A. *Essai d'une théorie sur la structure des cristaux appliquée à plusieurs genres de substances cristallisées*. Paris: Chez Gogné, 1783.
2. Wulff GZ. Zur Frage der Geschwindigkeit des Wachstums und der Auflösung der Kristallflächen. *Krist Min*. 1901;34:499-530.
3. Gibbs JW. *Collected Works*. New York: Longmans Green, 1906.
4. Donnay JDH, Harker D. A new law of crystal morphology, extending the law of Bravais. *Am Min*. 1937;22:151-155.
5. Bravais A. *Etudes Cristallographiques*. Paris: Gauthier-Villar, 1866.
6. Friedel MG. Etudes sur les lois de Bravais. *Bull Soc Fr Mineral*. 1907;30:326-455.
7. Hartman P, Perdok WG. On the relations between structure and morphology of crystals. I. *Acta Crystallogr*. 1955;8:49−52.
8. Hartman P, Perdok WG. On the relations between structure and morphology of crystals. II. *Acta Crystallogr*. 1955, 8, 521−524.
9. Hartman P, Perdok WG. On the relations between structure and morphology of crystals. III. *Acta Crystallogr*. 1955, 8, 525−529.
10. Meenan PA, Anderson SR, Klug DL. The influence of impurities and solvents on crystallization. In: Myerson AS. *Handbook of Industrial Crystallization*, *2nd ed*. Boston: Butterworth-Heinemann, 2001: 67-100.
11. Kuvadia ZB, Doherty MF. Reformulating multidimensional population balances for predicting crystal size and shape. *AIChE J*. 2013; 59 (9):3468-3474.
12. Kuvadia ZB, Doherty MF. Spiral growth model for faceted crystals of non-centrosymmetric organic molecules grown from solution. *Cryst Growth Des*. 2011;11(7):2780-2802.
13. Lovette MA, Doherty MF. Predictive modeling of supersaturation-dependent crystal shapes. *Cryst Growth Des*. 2012;12(2):656-669.
14. Sizemore JP, Doherty MF. A new model for the effect of molecular imposters on the shape of faceted molecular crystals. *Cryst Growth Des*. 2009;9(6):2637-2645.
15. Sizemore JP, Doherty MF. An engineering model for predicting the shape of solution-grown organic crystals in the presence of an additive. *VDI Berichte*. 2005;1901I(B-34):477-480.
16. Snyder RC, Doherty MF. Predicting crystal growth by spiral motion. *Proc R Soc A*. 2009;465(2104):1145-1171.
17. Winn D, Doherty MF. Predicting the shape of organic crystals grown from polar solvents. *Chem Eng Sci*. 2002;57:1805-1813.
18. Winn D, Doherty MF.A new technique for predicting the shape of solution-grown organic crystals. *AIChE J*. 1998;44(11):2501-2514.
19. Burton WK, Cabrera N, Frank FC. The growth of crystals and the equilibrium structure of their surfaces. *Phil Trans*. 1951;243(866):299-358.
20. Borsos A, Lakatos BG. Investigation and simulation of crystallization of high aspect ratio crystals with fragmentation. *Chem Eng Sci*. 2014;92:1133-1141.
21. Sato K, Nagai H, Hasegawa K, Tomori K, Kramer HJM, Jansen JP. Two-dimensional population balance model with breakage of high aspect ratio crystals for batch crystallization. *Chem Eng Sci*. 2008; 63:3271-3278.
22. Briesen H. Simulation of crystal size and shape by means of a reduced two-dimensional population balance model. *Chem Eng Sci*. 2006;61:104-112.
23. Gunawan R, Fusman I, Braatz RD. High resolution algorithms for multidimensional population balance equations. *AIChE J*. 2004; 50(11):2738-2749.
24. Ma CY, Wang XZ. Model identification of crystal facet growth kinetics in morphological population balance modeling of L-glutamic acid crystallization and experimental validation. *Chem Eng Sci*. 2012;70:22-30.
25. Ochsenbein DR, Schorsch S, Vetter T, Mazzotti M, Morari M. Growth rate estimation of β L-glutamic acid from online measurements of multidimensional particle size distributions and concentration. *Ind Eng Chem Res*. 2014;53:9136-9148.
26. Oullion M, Puel F, Févotte G, Righini S, Carvin P. Industrial batch crystallization of a plate-like organic product. In situ monitoring and 2D-CSD modeling. Part 2: kinetic modeling and identification. *Chem Eng Sci*. 2007;62:833-845.
27. Patience DB, Rawlings JB. Particle shape monitoring and control in crystallization processes. *AIChE J*. 2001;47(9):2125-2130.
28. Puel F, Marchal P, Klein JP. Habit transient analysis in industrial crystallization using two dimensional crystal size technique. *Trans IchemE*. 1997;75(A):193-205.
29. Puel F, Févotte G, Klein JP. Simulation and analysis of industrial crystallization processes though multidimensional population equations. Part 1.: a resolution algorithm based on the method of classes. *Chem Eng Sci*. 2003;58:3715-3727.
30. Matthews HB, Rawlings JB. Batch crystallization of a photochemical: modeling, control, and filtration. *AIChE J*. 1998;44(5):1119-1127.
31. Borchert C, Sundmacher K. Morphology evolution of crystal populations: modeling and observation analysis. *Chem Eng Sci*. 2012;70:87-98.
32. Shoji M, Takiyama H. The application of two-dimensional population balance model to study the effect of temperature profile on the crystal size distribution and aspect ratio. *Cryst Growth Des*. 2012;12: 5241−5246.
33. Derdour L, Skliar D. Crystallization from solutions containing multiple conformers. Part I. Modeling of crystal growth and supersaturation. *Cryst Growth Des*. 2012;12(11):5180-5187.
34. Kossel W. Zur Energetik von oberflächenvorgängen. *Ann Phys*. 1934;21:457−480.
35. Myerson AS, Ginde R. Crystals, crystal growth and nucleation. In: Myerson AS. *Handbook of Industrial Crystallization*, *2nd ed*. Boston, MA: Butterworth-Heinemann, 2001:33-65.
36. Chernov AA, Komatsu H. Topics in crystal growth kinetics. In: *Science and Technology of Crystal Growth*. Dordrecht: Kluwer Academic Publishers, 1995:67-80.
37. Mullin JW. *Crystallization*, *4th ed*. Oxford: Butterworth Heinemann, 2001.
38. Bennema P, Gilmer GH. Kinetics of crystal growth. In: Harman P. *Crystal Growth: An Introduction*. Amsterdam: North-Holland,1973: 263-327.
39. Winn D, Doherty MF. Modeling of crystal shape of organic materials grown from solution. *AIChE J*. 2000;46(7):1348-1367.
40. Garside J, Mersmann A, Nyvlt J. *Measurement of Crystal Growth and Nucleation Rates*, *2nd ed*. Rugby: IChemE, 2002.
41. Allen T. *Particle Size Measurement*, *4th ed*. New York: Chapman & Hall, 1990.
42. Besançon P, Frigot P, Lafaye JM, Lafaye A. Comparaison des mesures granulométriques par tamisage et microscopie optique:

statistique des mesodiametres. *Sci Tech Pharm*. 1985;1(6):508-515.
43. Garside J, Davey RJ. Secondary contact nucleation: kinetics, growth and scale-up. *Chem Eng Commun*. 1980;4(4-5):393-424.
44. Carr RL. Evaluating flow properties of solids. *Chem Eng*. 1965;72; 163-168.
45. Shah RB, Tawakkul MA, Khan MA. Comparative evaluation of flow for pharmaceutical powders and granules. *Pharm Sci Tech*. 2008; 9(1);250-258.

Appendix

The volume of a parallelepipedic crystal depicted in Figure A1 writes

$$V=\Psi(abc) \tag{A1}$$

where Ψ is the volume correction factor defined as

$$\Psi=\sqrt{1+2\cos(\alpha)\cos(\beta)\cos(\gamma)-\cos^2(\alpha)-\cos^2(\beta)-\cos^2(\gamma)} \tag{A2}$$

The angles between the three side of the crystals were determined from microscope image analysis and found to be approximately: $\alpha=\beta=1.15$ rad and $\gamma=1.99$ rad. On the basis of this data, the volume correction factor is $\Psi=0.61$.

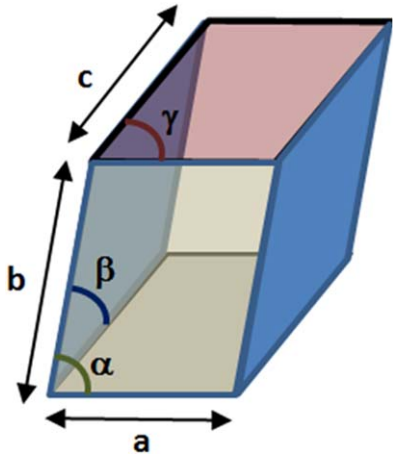

Figure A1. Characteristic dimensions and angles of an irregular parallelepiped.

[Color figure can be viewed in the online issue, which is available at wileyonlinelibrary.com.]

Manuscript received Mar. 30, 2015, and revision received June 26, 2015.